PAPER

Check for updates

Facile synthesis of a WO_x/Cs_yWO_3 heterostructured composite as a visible light photocatalyst†

N. Tahmasebi [ID] * and S. Madmoli

In this work, a WO_x/Cs_yWO_3 heterostructured composite was synthesized via a simple pyrolysis method followed by heat treatment under a reducing atmosphere. Optical absorption results revealed the WO_x/Cs_yWO_3 heterostructured composite exhibits a strong absorption tail in the Vis and NIR regions which could have important implications for its photoactivity. The photocatalytic performance of synthesized samples with different Cs/W molar ratios was evaluated by the photodegradation of RhB in aqueous solution under simulated solar light irradiation. The results revealed that the photocatalytic activity of the WO_x/Cs_yWO_3 composite is much higher than those of pure tungsten bronze (Cs_xWO_3, $x = 0.32$, and 0.5) and pure $WO_{2.83}$ samples, where 90% RhB was degraded after 160 min irradiation. Also, the WO_x/Cs_yWO_3 composite exhibits excellent photocatalytic activity for the degradation of MO, MB, RhB, and MG aqueous solution under visible light irradiation. It is proposed that the higher photocatalytic activity of the WO_x/Cs_yWO_3 composite could be attributed to the greater surface adsorption of dye molecules, intense light absorption in the visible and NIR regions, and photogenerated electron−hole separation.

1 Introduction

In recent years, semiconductor photocatalysis, owing to its ability to degrade organic dyes and contamination using solar energy, has attracted significant attention as a potential means to purify wastewater.[1,2] To date, the TiO_2 semiconductor is the most studied photocatalyst because its wide band gap ($\sim$3.2 eV) is suitable for photocatalytic performance under UV light irradiation.[3] However, the ultra violet (UV) region makes up a very small part of the total content of incoming solar energy, $\sim$5%, while the visible (Vis) and near-infrared (NIR) regions contain around 45%, and 50% of the total incoming energy.[4] Therefore, to avoid the huge waste of the visible part of solar light, the synthesis of visible light active photocatalysts has been highly desired. Tungsten oxide is an n-type semiconductor with a band gap between 2.4 and 2.8 eV that can degrade a wide range of organic contaminations under visible light irradiation.[5-7] However, because of rapid electron–hole recombination rate, stoichiometric WO_3 is often known as an insufficient photocatalyst under ambient condition.[6] Recently, to overcome this drawback, the photocatalyst activity of sub-stoichiometric tungsten oxide compound such as WO_x ($2 < x < 3$) has widely been investigated.[8,9] It is found that the sub-stoichiometric tungsten oxide exhibits noticeable activity in the photocatalytic degradation of dye molecules due to intense light

absorption in visible and near-infrared regions and strong surface adsorption of dye molecules.[8,10,11] Among all tungsten sub-oxide, monoclinic $W_{18}O_{49}$ has received considerable attention, and the adsorption and photocatalytic performance of other compounds rarely has been investigated.

Tungsten bronzes are a group of the non-stoichiometric compound with the general formula of M_xWO_3, (M represents an alkali metal) where x is in the range of $0 < x < 1$.[12] Tungsten bronze (M_xWO_3) nanostructures have a wide variety of application such as NIR shielding devises, gas sensors, photo-thermal, and photocatalyst owing to their excellent optical and electrical properties.[13-16] The crystal structures of this compound are based on corner sharing of WO_3 octahedra, with the metal cations located in the formed channels. Based on the nature of metal cations and its fractional occupancy in the channels, this compound can be classified into four type: perovskite tungsten bronze (PTB), tetragonal tungsten bronze (TTB), hexagonal tungsten bronze (HTB) and intergrowth tungsten bronze (ITB).[17,18] More recently, alkali tungstate and tungsten bronze have been regarded as photocatalyst. Up to now, only a few studies have been reported on the photocatalytic degradation of the organic compound by pure alkali tungstate and tungsten bronze.[19-21] Li et al. synthesized the Cs_xWO_3 nanorods that exhibited full-spectrum-response photocatalytic activity.[20] In 2010 by Wang et al. the photocatalytic activity of the sodium tungstate ($Na_xWO_{3+x/2}$) nanowires bundles was also reported, and the intrinsic mechanism of the enhanced photocatalytic activity was described based on "band-filling mechanism" and the existence of X^{5+}.[19] In other reports, the photocatalytic activity of pure alkali tungstate and tungsten

Department of Science, Jundi-Shapur University of Technology, Dezful, Iran. E-mail: tahmasebi@jsu.ac.ir

bronze is insignificant, and the coupling with other semi-conductor has been applied to improve the photocatalytic performance.[22–24] Man *et al.* prepared the $Cs_xWO_3/BiOCl$ heter-ojunction which showed a higher photocatalytic activity than that of a pure Cs_xWO_3 and pure BiOCl under visible light irra-diation.[24] However, the photocatalytic performance of tungsten bronzes is still poor, compared with other semiconductor photocatalyst. Also, up to now, although the hexagonal cesium tungsten bronze crystal structure extensively has been studied,[20] the experimental investigation of other cesium tungsten bronze crystal structures such as intergrowth tungsten bronze and cubic-pyrochlore phases rarely have been reported.[25–27]

To improve the photocatalyst performance of semi-conductors, a variety of strategies have been applied to suppress rapid combination of photogenerated electrons and holes, as well as to increase the intensity of absorbing light.[28] These include noble metal loading,[29] hydrogen treatment[30] and het-erojunction photocatalysts.[31] Among these, heterojunction photocatalysts have attracted most attention owing to their effectiveness for separation of photogenerated electron–hole pairs and more intense light absorption.[32–34] Heterojunction is the interface between two coupled semiconductors with unequal band structure.[31] It is reported that the heterojunction between different phases of same semiconductor photocatalyst is more effective for electrons–holes separation, due to the intimate contact of the two phase at atomic levels.[31] Zhang *et al.* synthesized a metallic/semiconductor H_xWO_3/WO_3 photo-catalyst which can degrade organic dyes under visible and NIR irradiation. The NIR absorption and the improvement of pho-tocatalytic activity were attributed to the oxygen vacancy levels below the conduction band of H_xWO_3 and electron transfer from WO_3 to H_xWO_3, respectively.[35] In 2015 by Cui *et al.* a WO_2/Na_xWO_3 composite phase was prepared by a high temperature reduction process of hexagonal-Na_xWO_3 nanowires bundles. The synthesized hybrid photocatalyst showed potential for IR-driven photocatalytic water splitting.[36] In this work, WO_x/Cs_yWO_3 heterostructured composites, the pure $WO_{2.83}$, and pure tungsten bronze (Cs_xWO_3, $x = 0.3$ and 0.50) were synthe-sized by a simple pyrolysis method followed by heat treatment under a reducing atmosphere (H_2/Ar 5%). The samples were characterized by scanning electron microscopy (SEM), X-ray diffraction (XRD), and UV-vis diffuse reflectance spectra. The effect of the initial molar ratio of Cs/W on the crystal structure, morphology and photocatalytic performance was investigated. The photocatalytic activities were evaluated by photo-degradation of rhodamine B (RhB) as pollutant model under light irradiation. It was found the photocatalytic activity of WO_x/Cs_yWO_3 composite was highly enhanced compared to the pure phase of tungsten bronzes (Cs_xWO_3, $x = 0.3$ and 0.66) and $WO_{2.83}$.

2 Experimental section

2.1 Synthesis of photocatalysts

All reagents used in this work were analytical grade and employed without further purification. Tungstic acid (H_2WO_4), hydrogen peroxide (H_2O_2), ammonia (NH_3), citric acid

($C_6H_8O_7$), cesium carbonate (Cs_2CO_3), polyvinylpyrrolidone, methylene blue (MB), rhodamine B (RhB), methyl orange (MO), and malachite green (MG) were purchased from Sigma-Aldrich. In a typical experimental, 0.76 g tungstic acid powder was loaded into a beaker, and then 4.5 mL hydrogen peroxide was poured into the beaker and was stirred at 50 °C for 1 h. Then, 1 mL of NH_3 and 2 g citric acid was added to the above solution under vigorous stirring for 30 min. After that, different amount of cesium carbonate was added and followed by constant stir-ring for 30 min. The initial molar ratio of Cs/W was set to be 0.00, 0.10, 0.30, and 0.66. Finally, 0.02 g polyvinylpyrrolidone (PVP, $M_w = 1\,300\,000$) was added to the solution. The solution was stirred for 14 h to obtain a homogeneous sol. Then, the obtained sol was transferred into a crucible and thermal decomposition was done with a heating rate of 1 °C min^{-1} for 8 h from the room temperature in the air, and followed by heat treatment at 500 °C for 2 h. Finally, the synthesized powder samples with different Cs/W molar ratio were annealed in a hydrogen atmosphere ($H_2/Ar = 5\%$) at the temperature of 650 °C for 1 h with the flow of hydrogen at 10 mL h^{-1} to get the final product.

2.2 Characterization

Scanning electron microscopy (TESCAN VEGA model) and field emission scanning electron microscopy (TESCAN MIRA3 XMU-FESEM) were utilized to study the morphology and micro-structure of the samples and to determine the chemical composition with energy dispersive X-ray spectroscopy (EDS) spectrum. X-ray diffraction (XRD) with Cu Kα radiation ($\lambda = 1.54178$ Å) at 40 kV was used to study the crystalline phases. The UV-vis diffuse reflectance spectra were measured by UV-vis spectrometer (Avaspec-2048-TEC model, Avantes) using $BaSO_4$ as a reference in the range of 200–800 nm. The absorption spectra were obtained by kubelka–Munk method. The photo-luminescence (PL) emission spectra were performed with spectrometer (Thermo Lumia model) at room temperature with the excitation wavelength of 260 nm.

2.3 Photocatalytic and adsorption experiments

The photocatalytic performance of the synthesized samples with different Cs/W molar ratio in the degradation of RhB was evaluated by using a 55 W xenon lamp as simulated solar light source. In a typical experiment, 60 mg photocatalyst was dispersed in 60 mL of RhB solution (25 mg L^{-1} for $WO_{2.83}$ and WO_x/Cs_yWO_3 samples, and 5 mg L^{-1} for $Cs_{0.3}WO_3$ and $Cs_{0.5}WO_3$ samples) in a 250 mL beaker reactor that was equip-ped with a water-cooling jacket to adjust the reaction temper-ature. The lamp located 10 cm away from the reaction solution. Also, the visible light activity of photocatalysts was investigated by photocatalytic degradation of an aqueous solution of RhB, MG, and MB (40 mL, 20 mg L^{-1}) in the presence of 40 mg photocatalyst and MO (40 mL, 20 mg L^{-1}) in the presence of 20 mg photocatalyst under a white light LED lamp (30 W). Prior to light irradiation (xenon or LED), the solution was magneti-cally stirred in the dark for 80 min to reach a complete adsorption–desorption equilibrium between the photocatalyst

and pollutant model. During the light irradiation, at given interval, 2 mL of solution was sampled and centrifuged to remove the photocatalyst. The residual pollutant concentrations were estimated by the UV-vis spectrophotometer measurement. The photodegradation of the pollutant model solution was estimated according to the following formula: $\eta = [(C_0 - C)/C_0] \times 100\%$, where C and C_0 are the absorbance of the pre- and post-irradiation of the RhB solution, respectively.

To compare the dye adsorption capability of the synthesized samples, 60 mg photocatalyst was dispersed in 60 mL of RhB solution (5 mg L^{-1}) in the dark, and the solution was magnetically stirred. Then at given interval 2 mL of solution was collected and centrifuged, and the RhB concentration was determined by UV-vis spectroscopy.

3   Results and discussion

3.1   XRD analysis

The crystal structures of products synthesized with initial Cs/W molar ratio of $A = 0.00$, 0.10, 0.30 and 0.66 were characterized by XRD pattern. As shown in Fig. 1, all the diffraction peaks of the synthesized samples with $x = 0.00$ and $x = 0.30$ could be indexed to pure monoclinic $WO_{2.83}$ phase ($W_{24}O_{68}$, JCPDS no. 36-0103) and pure hexagonal $Cs_{0.32}WO_3$ phase (JCPDS no. 83-1334), respectively. Fig. 1(b) exhibits when the initial Cs/W molar ratio is 0.10, two series of diffraction peaks can be observed that attributed to the monoclinic phase of $WO_{2.83}$ (JCPDS no. 36-0103) and orthorhombic $Cs_{0.069}WO_3$ phase (JCPDS no. 83-2120). Therefore, this sample shows a mixed phase of monoclinic-$WO_{2.83}$ and orthorhombic-$Cs_{0.069}WO_3$. Fig. 1(d) shows the XRD pattern of the synthesized sample with $A = 0.66$. This figure clearly displays that all the diffraction peaks can be indexed to pyrochlore-type cubic $Cs_{0.5}WO_3$ phase (JCPDS no. 81-1259). Therefore, it can be concluded that the

Fig. 1   XRD patterns of synthesized samples with different cesium to tungsten molar ration ($A = Cs/W$): (a) 0.00, (b) 0.10, (c) 0.30, and (d) 0.66.

synthesized samples with initial $A = Cs/W$ molar ratio of $A = 0.00$, 0.10, 0.30 and 0.50 are denoted as m-$WO_{2.83}$, m-WO_x/O-Cs_yWO_3, h-$Cs_{0.32}WO_3$ and c-$Cs_{0.5}WO_3$, respectively.

3.2   Morphological analysis

3.2.1   SEM analysis. The morphology of samples were observed by SEM analysis. Fig. 2 shows the morphology of synthesized tungsten bronze samples with different initial cesium to tungsten molar ratio. As shown in Fig. 2(a), the sample without cesium content (m-$WO_{2.83}$) exhibits large nanosheets with a rather smooth surface and the average size of several micrometers. The morphology of $WO_{2.83}/Cs_{0.069}WO_3$ mixed phase has formed of a series of microsheets while a large number of nanoparticles with an average size of 200 nm have been embodied within these microsheets (Fig. 2(b and c)). The morphology of pure hexagonal tungsten bronze ($Cs_{0.32}WO_3$) presents only uniform nanoparticles with an average size of about 400 nm (Fig. 2(d and e)). Thus, the observed nanoparticles in the $WO_{2.83}/Cs_{0.069}WO_3$ structure could be related to the orthorhombic tungsten bronze phase ($Cs_{0.06}WO_3$), so that at higher Cs/W molar ration (Cs/W > 0.1) almost all WO_3 structure have transformed into cesium tungsten bronze nanoparticles. Furthermore, the morphology of synthesized sample with initial molar ration of Cs/W = 0.66 have irregular particles with size of 200–800 nm that have a pure cubic crystal phase ($Cs_{0.5}WO_3$).

3.2.2   EDS analysis. The EDS analysis was used to determine the chemical composition of the synthesized samples with initial Cs/W molar ratio of $A = 0$, 0.10, 0.30 and 0.66 (Fig. S1†). This analysis revealed that the samples are composed of W, O and Cs elements, and other impurities is not detected. Also, this analysis was carried out to calculate the value of x in Cs_xWO_3 samples according to atomic percent of W and Cs. It is found that the calculated atomic ratio of Cs/W is equal to 0.00, 0.08, 0.31 and 0.58 for pure tungsten oxide and synthesized samples with initial Cs/W molar ration of 0.10, 0.30 and 0.66, respectively (Table 1), which are very close to the determined phases based on XRD results. Furthermore, to reveal the elemental distribution of elements, the elemental mapping is performed on synthesized sample with initial Cs/W molar ration of 0.10. This analysis reveals the highly uniform distribution of Cs and W elements on a microsheet (Fig. 3). Therefore, based on XRD and mapping results it can be expected that $WO_{2.83}$ and Cs_xWO_3 are successfully composited and formed a $WO_{2.83}/Cs_xWO_3$ mixed phase.

3.3   Photocatalytic and adsorption study

To understand the relationship between tungsten bronze crystal phase and photocatalyst performance, the photocatalytic activity of synthesized samples was evaluated by the photocatalytic decomposition of RhB in an aqueous solution as a model pollutant under simulated solar light (xenon, 55 W), and visible light (white light LED, 30 W) sources. Temporal evolution of UV-vis absorption spectra of RhB solution in the presence of WO_x/Cs_yWO_3 composite and $Cs_{0.5}WO_3$ photocatalysts under simulated sunlight are displayed in Fig. 4(A and B). In this figure, the decrease in the absorption peak at

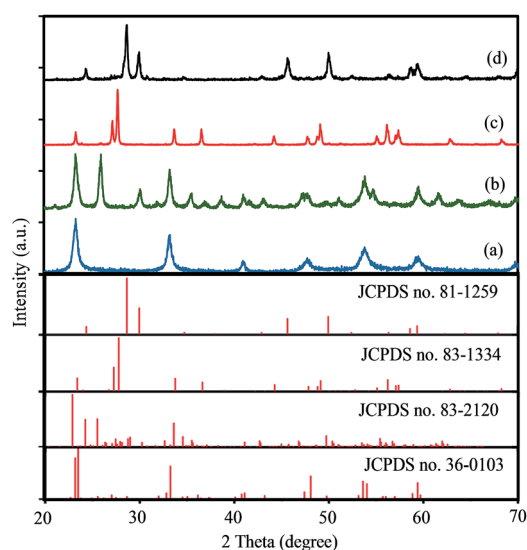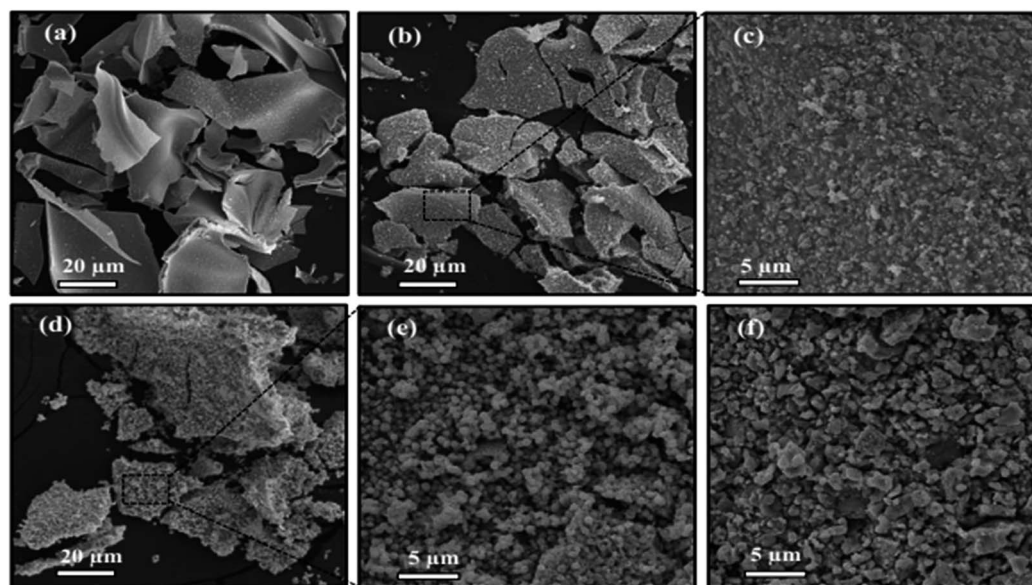**Fig. 2** SEM images of synthesized samples with different cesium to tungsten molar ration (x = Cs/W): (a) x = 0.00, (b, c) 0.10, (d, e) 0.30, and (f) 0.66.

Table 1 The EDS analysis of synthesized samples with initial Cs/W molar ratio of A = 0, 0.10, 0.30 and 0.66

Initial Cs/W molar ratio	Atomic percent (%)			Estimated Cs/W atomic ratio by EDS
	OK	WL	CsL	
x = 0.00	67.14	32.86	—	—
x = 0.10	72.65	25.33	2.03	0.08
x = 0.30	70.35	22.62	7.03	0.31
x = 0.66	72.51	17.32	10.17	0.58

~550 nm, accompanied by the exposure time, can be related to the removal of the RhB molecules in the solution. Fig. 4(C) shows the photocatalyst efficiencies of the samples under

Fig. 3 FESEM image of $WO_{2.83}/Cs_{0.069}WO_3$ composite (a), and its corresponding elemental mappings of (b) Cs, (c) O, and (d) W elements.

simulated solar light, where C and C_0 were the absorption of RhB at the wavelength of 550 nm and the absorption after the adsorption equilibrium on the photocatalyst before irradiation. This figure displays that only 14%, 16% and 18% RhB can be degraded by pure $WO_{2.83}$, $Cs_{0.32}WO_3$ and $Cs_{0.5}WO_3$, respectively, while WO_x/Cs_yWO_3 composite sample with a phase junction could degraded 90% RhB after 160 min irradiation. Furthermore, the plot of $\ln(C_0/C)$ *versus* irradiation time (t) displays a linear relation (Fig. S2†). Thus, the photodegradation reaction follows a pseudo-first order kinetic reaction; $\ln(C_0/C) = kt$, where C and C_0 are the RhB concentration at initial and after t min irradiation, respectively, and k is the RhB photodegradation rate constant. The reaction rate constants were presented in Fig. 4(D). As shown in this figure, the photocatalytic activity of $WO_{2.83}/Cs_{0.07}WO_3$, with k = 0.05 cm^{-1}, is much higher than those of other samples.

Then, the visible-light driven photocatalytic activity of WO_x/Cs_yWO_3 composite was evaluated by photocatalytic degradation of several types of dyes. Fig. S3† shows the absorption spectra of MO, MB, RhB, and MG solution (20 mg L^{-1}) over time after light irradiation with a white light LED (30 W) used as a visible light source in the presence of WO_x/Cs_yWO_3 composite as the photocatalyst. As shown in Fig. 5(b), the photodegradation efficiencies of MO, MB, RhB, and MG molecules in the presence of photocatalyst after 160 min irradiation were 96%, 95%, 83%, and 98%, respectively. In contrast, the photodegradation of MO, RhB, and MG solution in the absence of any photocatalyst under visible light illumination was insignificance, and 23% of MB will be degraded under same condition. These results confirmed the good visible light activity of the composite phase for photocatalytic degradation of various dyes. Furthermore, the SEM images of the WO_x/Cs_yWO_3 composite photocatalyst before and after photocatalytic reaction to photodegrade RhB molecules (under visible light irradiation) were employed to
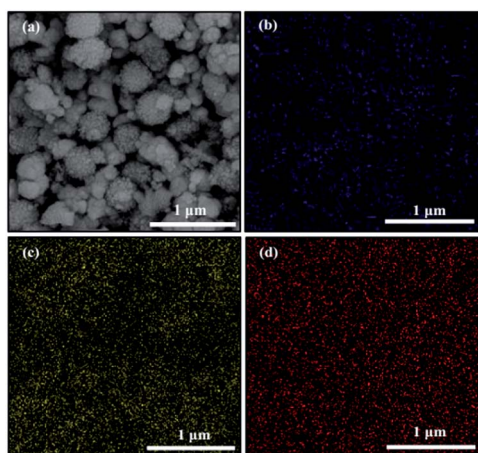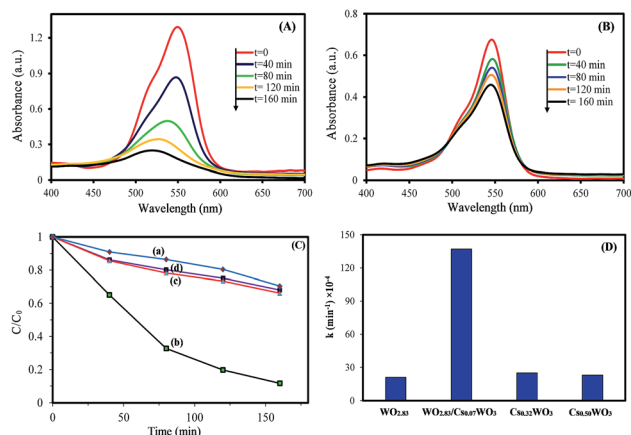
Fig. 4 The temporal evolution of UV-vis absorption spectra of RhB solution in the presence of (A) $WO_{2.83}/Cs_{0.07}WO_3$ composite, and (B) $Cs_{0.50}WO_3$ under simulated sunlight (xenon lamp), (C) photocatalytic degradation of RhB in the presence of (a) $WO_{2.83}$, (b) WO_x/Cs_yWO_3 composite, (c) $Cs_{0.32}WO_3$, and (d) $Cs_{0.50}WO_3$, and (D) photodegradation rate constant of them.

confirm its stability (Fig. S4†). The results confirm that not significant changes occurred after the photocatalytic reactions. Moreover, the WO_x/Cs_yWO_3 composite photocatalyst exhibits good stability for photodegradation of RhB under visible light irradiation after three cycles (Fig. 5(b)).

It is well known that the important factors on photocatalytic activity of a semiconductor are dye adsorption ability, light absorption for the electron–hole generation, and electron–hole separation. To study the influence of the dye adsorption ability on the photocatalyst activity of synthesized samples, the adsorption capacity of RhB on synthesized samples was investigated. Firstly, 50 mg of samples were added into 50 mL of RhB solution (5 mg L^{-1}), then the solution was magnetically stirred in the dark for 80 min to reach a complete adsorption–desorption equilibrium between the photocatalyst and RhB. Fig. 6(A) shows the change of UV-vis absorption spectra of RhB solution in the presence of $WO_{2.83}/Cs_{0.07}WO_3$ composite during adsorption. It can be seen that the intensity of absorption peak decreases with increasing the adsorption time under dark condition. Fig. 6(B) presents the evolution of the bronze samples as a function of adsorption time. This figure clearly
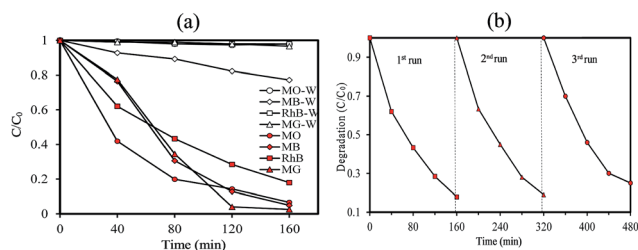

Fig. 5 (a) The photocatalytic degradation of MG, RhB, MB, and MO solution (20 mg L^{-1}) in the absence and in the presence of WO_x/Cs_yWO_3 composite, and (b) recycle experiment in the photocatalytic degradation of RhB in the presence of WO_x/Cs_yWO_3 composite under visible light irradiation (LED 30 W).
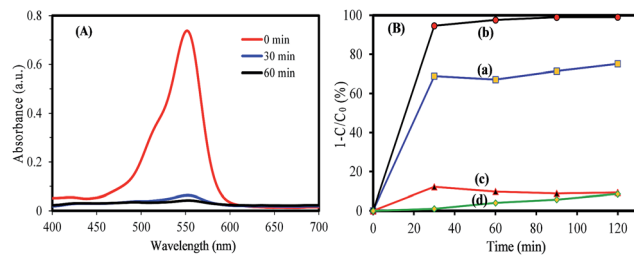

Fig. 6 (A) UV-visible absorption spectra of a solution of RhB (50 mL, 5 mg L^{-1}) in the presence of WO_x/Cs_yWO_3 composite, and (B) adsorption percent of RhB on the (a) $WO_{2.83}$, (b) WO_x/Cs_yWO_3 composite, (c) $Cs_{0.32}WO_3$, and (d) $Cs_{0.50}WO_3$.

exhibits that almost 98% RhB were removed by WO_x/Cs_yWO_3 within 30 min in dark condition. This value is much higher that the adsorption capacity of $WO_{2.83}$ (~75%). In addition, the Cs_xWO_3 samples with $x = 0.32$ and 0.50 exhibit weak adsorption capacity (~8% and 7%, respectively). Therefore, WO_x/Cs_yWO_3 and pure $WO_{2.83}$ sample have a much stronger dye adsorption capacity, while other Cs_xWO_3 samples ($x = 0.32$ and 0.50) have a weak adsorption capacity. To measure the specific surface area of the samples, the N_2 adsorption–desorption curves were performed. The results are shown in Fig. S5 and Table S1.† This analysis indicated that the specific surface area of all samples is similar and insignificant (less than 4 m^2 g^{-1}). Thus, the rapid RhB adsorption of WO_x/Cs_yWO_3 (~100%) and $WO_{2.83}$ (~75%) in comparison to other Cs_xWO_3 samples (<8%) ($x = 0.3$ and 0.66) may be attributed to the presence of surface oxygen vacancies and the strong electrostatic attraction.[37,38]

The light absorption for electron–hole generation is another key factor that has a significant effect on photocatalysis performance of a semiconductor. Therefore, the optical properties of synthesized samples have been investigated. The synthesized samples exhibit a blue color that the color gradually changes to a dark blue color ($Cs_{0.50}WO_3$) with increasing Cs/W molar ratio (Fig. S6†). The strong blue color could be related to the intense light absorption ability that is useful to create electron–hole pairs.[39] Fig. 7(A) displays the UV-vis absorption spectra of $WO_{2.83}$, pure tungsten bronze samples (Cs_xWO_3: $x = 0.32$, and 0.50), and WO_x/Cs_yWO_3 composite. It is observed that in addition to the absorption in UV region, all samples exhibit strong absorption in the visible region. Furthermore, one can observe the WO_x/Cs_yWO_3 composite sample exhibits more
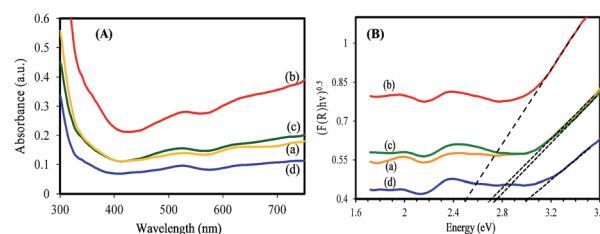

Fig. 7 (A) UV-vis absorption spectra (converted from DRS spectra) and (B) the plot of $(F(R)h\nu)^{1/2}$ vs. $h\nu$ of (a) $WO_{2.83}$, (b) WO_x/Cs_yWO_3 composite, (c) $Cs_{0.32}WO_3$, and (d) $Cs_{0.50}WO_3$ samples.

intense light absorption that can be attributed to the strong interaction between $WO_{2.83}$ and $Cs_{0.069}WO_3$ phases. The optical band gap of the samples is obtained from the equation: $(F(R)h\nu)^n = B(E - E_g)$, where $F(R)$ is the kubelka–Munk function, $h\nu$ is the photon energy, B is a constant and n is 2 or 1/2 for direct or indirect transition, respectively. The E_g value is determined by extrapolating the linear region of $(Ah\nu)^{1/2}$ plot to $h\nu = 0$. It is found that the energy gap of Cs_yWO_3 pure phase shows a blue shift with increasing x value. Fig. 7(B) indicates that the energy gap of pure $WO_{2.83}$, $Cs_{0.32}WO_3$ and $Cs_{0.5}WO_3$ phases are approximately 2.70 eV, 2.75 and 3.00 eV, respectively. However, the band gap value of WO_x/Cs_yWO_3 composite phase is esti-mated to be 2.50 eV. The relatively low-value band gap of composite phase compared to pure phases can be attributed to the coupling of $WO_{2.83}$ and $Cs_{0.069}WO_3$ phases and strong interaction between them.[32,40]

It is well known that the oxygen vacancies in sub-stoichiometric tungsten oxide can produce unoccupied local-ized states within the forbidden gap (Fig. 8(a)) that act as elec-tron acceptor.[9,11] On the other hand, when Cs molecules are doped into WO_3 lattice these molecules are dissociated as Cs ions and electrons ($Cs, Cs^+ + e^-$). The Cs ions are localized in the tungsten oxide structural tunnels and weakly bounded to the WO_6 octahedral. Also, the induced electrons are trapped in the unoccupied d-orbital of the W^{6+} and reduced it to W^{5+}, and also the lattice will be distorted by repelling and attracting the surrounding negative (O^{2-}) and positive (W^{6+}) ions.[13,41] The lattice distortion can produce a series of localized states below the conduction band (CB) as polaron states (Fig. 8(b and c)). It is expected that initially, the donated electrons from Cs atoms occupied the polaron states below the conduction band (Fig. 8(b)), and as Cs in the structure increases, based on band-filling mechanism some of the states within the CB are then filled, (Fig. 8(c), process 1).[19] As a result, the band gap energy of highly doped tungsten bronze ($Cs_{0.5}WO_3$) increases compared with the other samples (Fig. 7(B)). According to the above mentioned explains, as illustrated in Fig. 8, the Vis and NIR light absorption ($\lambda < 1100$ nm) of Cs_xWO_3 (or $WO_{2.83}$) is sug-gested to be due to electron transition from VB to the polaron states (or localized states) (process 2) and from polaron state (or localized states) to the CB (process 3), or by electron transition between neighbor W^{5+} and W^{6+} sites.[4,41,42] Besides, the induced electrons can also be inserted as free electrons in the conduc-tion band and absorbed the long wavelength of NIR ($\lambda > 1100$ nm) by LSPR of free electrons.[42]
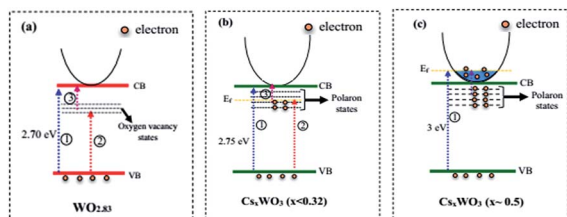

Fig. 9 PL spectra of (a) $WO_{2.83}$, (b) WO_x/Cs_yWO_3 composite, (c) $Cs_{0.32}WO_3$, and (d) $Cs_{0.50}WO_3$ samples.

To investigate the charge separation ability of synthesized samples, the photoluminescence (PL) emission spectra were recorded at room temperature. As shown in Fig. 9, the PL spectra of all samples display that no PL signal could be observed in the wavelength range of 450–550 nm, demon-strating that no photogenerated electron–hole recombination occurred during the photocatalytic degradation process under visible light irradiation. These results confirm that tungsten bronze is helpful to enhance the charge separation process, which may be attributed to the polarons and oxygen vacancies states within the band gap.[43]

To describe the mechanism of enhanced photocatalytic activity of WO_x/Cs_yWO_3 composite the radical-trapping experi-ments and relative band positions were carried out. In this study, ethylene diamine tetra acetic acid disodium (EDTA-2Na), $K_2Cr_2O_7$, and tert-butyl alcohol (TBA) were employed as scav-engers of h^+, e^-, and hydroxyl radical ($^\bullet OH$), respectively. As shown in Fig. 10, when EDTA-2Na selected as the scavenger, the photodegradation of RhB significantly decreases, while in the presence of $K_2Cr_2O_7$ as scavenger the photocatalytic degrada-tion of RhB slightly decreased. Moreover, when TBA is added as hole scavenger the photocatalytic degradation performance of RhB by WO_x/Cs_yWO_3 is not affected, revealing $^\bullet OH$ radicals don't take part in the photocatalytic degradation of RhB. These results suggest that although both the photogenerated electrons and holes take part in the photocatalytic reaction, the holes (h^+)

Fig. 8 Schematic representation of band structure of (a) $WO_{2.83}$, (b) $WO_{2.83}/Cs_xWO_3$ ($x < 0.32$), and (c) Cs_xWO_3 samples ($x \sim 0.5$).

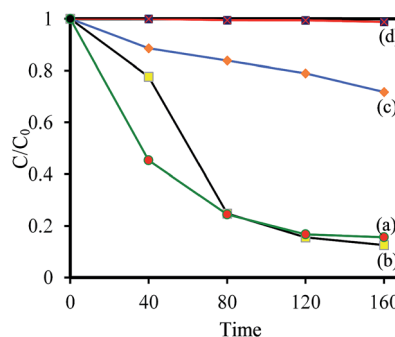Fig. 10 Effects of different scavengers: (a) no scavenger, (b) TBA, (c) $K_2Cr_2O_7$, and (d) EDTA-2Na on the photocatalytic degradation of RhB by WO_x/Cs_yWO_3 composite photocatalyst under Xe light irradiation.

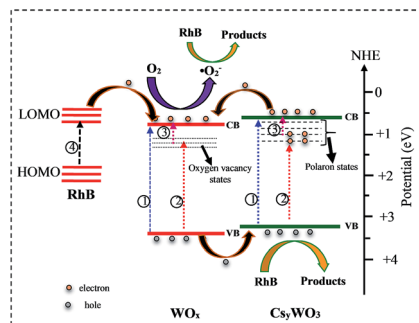**Fig. 11** A schematic sketch of the photocatalysis mechanism of WO_x/Cs_yWO_3 composite.

plays the important role in the degradation of RhB over WO_x/Cs_yWO_3 semiconductor photocatalyst.

Furthermore, the valance band (VB) and the conduction band (CB) position of WO_x and Cs_yWO_3 are calculated using the following two equations.[44,45]

$$E_{CB} = X - E_e - 0.5E_g \tag{1}$$

$$E_{VB} = E_{CB} + E_g \tag{2}$$

where E_{CB} and E_{VB} are the CB and VB edge potential, respectively, X is the absolute electronegativity of the semiconductor, E_e is the energy of free electrons *vs.* hydrogen (4.5 eV), and E_g is the band gap energy of semiconductor. The X values for $WO_{2.83}$ and $Cs_{0.069}WO_3$ are 6.53 eV and 6.41 eV, respectively. Based on the DRS results, the band gap of $WO_{2.83}$ and $Cs_{0.069}WO_3$ are considered as ~2.70 eV and ~2.75 eV, respectively. Therefore, the bottom of the CB and the top of the VB of the $WO_{2.83}$ are 0.68 eV and 3.38 eV, respectively, and the CB and VB of the $Cs_{0.069}WO_3$ are estimated to be 0.56 eV and 3.26 eV, respectively. Therefore, as shown in Fig. 11, the WO_x/Cs_yWO_3 composite exhibits a type-2 heterostructure.[31] As a result, the photogenerated electrons in the CB of $Cs_{0.07}WO_3$ can be transferred to the CB of WO_x, and inversely the photogenerated holes in the VB of $WO_{2.83}$ are transferred to the VB of Cs_yWO_3. Thus, the photogenerated electrons and holes are effectively separated, which is beneficial to suppress electron–hole recombination, and as a result can significantly enhance the photocatalytic activity. On the other hand, the RhB molecules can also be excited to form RhB* under visible light irradiation (Fig. 11, process 4). Then, the adsorbed RhB* molecules on the photocatalyst surface could transfer electrons to the CB of $WO_{2.83}$, and react with the adsorbed O_2 molecules to generate $\cdot O_2$ radicals, which would be considered as part of photodegradation activity under visible light irradiation.

4 Conclusions

In summary, we fabricated pure $WO_{2.83}$, pure cesium tungsten bronze (Cs_xWO_3 $x = 0.32$ and 0.50) and a WO_x/Cs_yWO_3 heterostructured composite by a simple pyrolysis method. The crystal structure and microstructure of the samples were

investigated by XRD and SEM analysis. The photocatalytic activity of synthesized samples was evaluated by the photodegradation of RhB in an aqueous solution as a model pollutant. The results revealed that the monoclinic/orthorhombic $WO_{2.83}$/$Cs_{0.069}WO_3$ composite shows higher photocatalytic activity compared to the pure $WO_{2.83}$ and pure tungsten bronze phase (Cs_xWO_3, $x = 0.32$ and 0.50). Moreover, the WO_x/Cs_yWO_3 composite displays excellent photocatalytic activation under visible light irradiation, the photodegradation efficiencies of MO, MB, RhB, and MG molecules in the presence of photocatalyst after 160 min visible light irradiation (white light LED lamp) were 96%, 95%, 83%, and 98%, respectively. The enhanced photocatalytic performance of WO_x/Cs_yWO_3 composite sample is attributed to the strong dye adsorption capability, intense light absorption, and effective separation of electron–hole pairs which could be attributed to the surface oxygen vacancies, polaron states below the conduction band, and the strong interaction between $WO_{2.83}$ and $Cs_{0.069}WO_3$ phases, respectively.

Conflicts of interest

There are no conflicts to declare.

Notes and references

1 M. Zhang, Z. Lian, Y. Wang and S. Pan, *RSC Adv.*, 2016, **6**, 39234–39239.

2 X. N. Song, C. Y. Wang, W. K. Wang, X. Zhang, N. N. Hou and H. Q. Yu, *Adv. Mater. Interfaces*, 2016, **3**, 1500417.

3 Y. Sang, H. Liu and A. Umar, *ChemCatChem*, 2015, **7**, 559–573.

4 X. Wu, J. Wang, G. Zhang, K. I. Katsumata, K. Yanagisawa, T. Sato and S. Yin, *Appl. Catal., B*, 2017, **201**, 128–136.

5 C. Cheng, J. Shi, Y. Hu and L. Guo, *Nanotechnology*, 2017, **28**, 164002.

6 S. Cong, F. Geng and Z. Zhao, *Adv. Mater.*, 2016, **28**, 10518–10528.

7 S. Zhang, H. Li and Z. Yang, *J. Alloys Compd.*, 2017, **722**, 555–563.

8 J. Liu, O. Margeat, W. Dachraoui, X. Liu, M. Fahlman and J. Ackermann, *Adv. Funct. Mater.*, 2014, **24**, 6029–6037.

9 J. Yan, T. Wang, G. Wu, W. Dai, N. Guan, L. Li and J. Gong, *Adv. Mater.*, 2015, **27**, 1580–1586.

10 J. Qian, Z. Zhao, Z. Shen, G. Zhang, Z. Peng and X. Fu, *RSC Adv.*, 2016, **6**, 8061–8069.

11 H. L. Guo, Q. Zhu, X. L. Wu, Y. F. Jiang, X. Xie and A. w. Xu, *Nanoscale*, 2015, **7**, 7216–7223.

12 O. Zivkovic, C. Yan and M. J. Wagner, *J. Mater. Chem.*, 2009, **19**, 6029–6033.

13 X. Wu, S. Yin, D. Xue, S. Komarneni and T. Sato, *Nanoscale*, 2015, **7**, 17048–17054.

14 T. A. Martins, T. R. Machado, M. M. Ferrer, S. M. Zanetti and E. Longo, *Mater. Lett.*, 2016, **185**, 197–200.

15 W. Guo, C. Guo, N. Zheng, T. Sun and S. Liu, *Adv. Mater.*, 2017, **29**, 1601694.

16 G. Cui, W. Wang, M. Ma, J. Xie, X. Shi, N. Deng, J. Xin and B. Tang, *Nano Lett.*, 2015, **15**, 7199–7203.

17 J. S. Lee, H. C. Liu, G. D. Peng and Y. Tseng, *J. Cryst. Growth*, 2017, **465**, 27–33.

18 A. Hussain, Phase Analyses of Potassium, *Acta Chem. Scand., Ser. A*, 1978, **32**, 479–484.

19 L. Wang, J. Zhan, W. Fan, G. Cui, H. Sun, L. Zhuo, X. Zhao and B. Tang, *Chem. Commun.*, 2010, **46**, 8833–8835.

20 G. Li, C. Guo, M. Yan and S. Liu, *Appl. Catal., B*, 2016, **183**, 142–148.

21 X. Wang, L. Pang, X. Hu and N. Han, *J. Environ. Sci.*, 2015, **35**, 76–82.

22 T. Liu, B. Liu, J. Wang, L. Yang, X. Ma, H. Li, Y. Zhang, S. Yin, T. Sato, T. Sekino and Y. Wang, *Sci. Rep.*, 2016, **6**, 27373.

23 X. Huang, J. X. Liu, F. Shi, L. Yu and S. H. Liu, *Mater. Des.*, 2016, **110**, 624–632.

24 H. Man, C. Wang, Y. Sun, Y. Ning, P. Song and W. Huang, *Journal of Materiomics*, 2016, **2**, 338–343.

25 A. Hussain and L. Kihlborg, *Theor. Gen. Crystallogr.*, 1976, **32**, 551–557.

26 N. Tahmasbi, S. Madmoli and P. Farahnak, *Mater. Lett.*, 2017, **211**, 161–164.

27 R. J. Cava, R. S. Roth, T. Siegrist, B. Hessen, J. J. Krajewski and W. F. Peck, *J. Solid State Chem.*, 1993, **103**, 359–365.

28 X. Chen, L. Liu, Y. Y. Peter and S. S. Mao, *Science*, 2011, **331**, 746–750.

29 X. Hu, J. Tian, Y. Xue, Y. Li and H. Cui, *ChemCatChem*, 2017, **9**, 1511–1516.

30 G. Wang, H. Wang, Y. Ling, Y. Tang, X. Yang, R. C. Fitzmorris, C. Wang, J. Z. Zhang and Y. Li, *Nano Lett.*, 2011, **11**, 3026–3033.

31 J. Low, J. Yu, M. Jaroniec, S. Wageh and A. A. Al-Ghamdi, *Adv. Mater.*, 2017, DOI: 10.1002/adma.201601694.

32 Y. Sun, W. Wang, L. Zhang and Z. Zhang, *Chem. Eng. J.*, 2012, **211**, 161–167.

33 Y. Li, Z. Tang, J. Zhang and Z. Zhang, *Appl. Catal., B*, 2017, **207**, 207–217.

34 Y. Kong, H. Sun, X. Zhao, B. Gao and W. Fan, *Appl. Catal., A*, 2015, **505**, 447–455.

35 L. Zhang, W. Wang, S. Sun and D. Jiang, *Appl. Catal., B*, 2015, **168**, 9–13.

36 G. Cui, W. Wang, M. Ma, J. Xie, X. Shi, N. Deng, J. Xin and B. Tang, *Nano Lett.*, 2015, **15**, 7199–7203.

37 D. R. Jones, V. Gomez, J. C. Bear, B. Rome, F. Mazzali, J. D. McGettrick, A. R. Lewis, S. Margadonna, W. A. Al-Masry and C. W. Dunnill, *Sci. Rep.*, 2017, **7**, 4090.

38 Z. Lou and C. Xue, *CrystEngComm*, 2016, **18**, 8406–8410.

39 X. Xu, C. Randorn, P. Efstathiou and J. T. Irvine, *Nat. Mater.*, 2012, **11**, 595.

40 N. Wetchakun, S. Chaiwichain, B. Inceesungvorn, K. Pingmuang, S. Phanichphant, A. I. Minett and J. Chen, *ACS Appl. Mater. Interfaces*, 2012, **4**, 3718–3723.

41 K. Adachi and T. Asahi, *J. Mater. Res.*, 2012, **27**, 965–970.

42 X. Wu, S. Yin, D. Xue, S. Komarneni and T. Sato, *Nanoscale*, 2015, **7**, 17048–17054.

43 X. Han, S. Dong, C. Yu, Y. Wang, K. Yang and J. Sun, *J. Alloys Compd.*, 2016, **685**, 997–1007.

44 J. Yu, Y. Wang and W. Xiao, *J. Mater. Chem. A*, 2013, **1**, 10727–10735.

45 M. Mousavi, A. Habibi-Yangjeh and M. Abitorabi, *J. Colloid Interface Sci.*, 2016, **480**, 218–231.